

Pathways towards break even for low convergence ratio direct-drive inertial confinement fusion

R.W. Paddock^{1,†}, H. Martin², R.T. Ruskov², R.H.H. Scott³, W. Garbett⁴,
B.M. Haines⁵, A.B. Zylstra⁶, E.M. Campbell⁷, T.J.B. Collins⁷,
R.S. Craxton⁷, C.A. Thomas⁷, V.N. Goncharov⁷, R. Aboushelbaya¹,
Q.S. Feng¹, M.W. von der Leyen¹, I. Ouatu¹, B.T. Spiers¹, R. Timmis¹,
R.H.W. Wang¹ and P.A. Norreys^{1,2,3}

¹Department of Physics, Atomic and Laser Physics Sub-Department, Clarendon Laboratory, University of Oxford, Parks Road, Oxford, Oxfordshire OX1 3PU, UK

²University College, University of Oxford, High Street, Oxford, Oxfordshire OX1 4BH, UK

³Rutherford Appleton Laboratory, Central Laser Facility, STFC, Harwell Campus, Didcot, Oxfordshire OX11 0QX, UK

⁴AWE plc, Aldermaston, Reading, Berkshire RG7 4PR, UK

⁵Los Alamos National Laboratory, MS T087, Los Alamos, NM 87545, USA

⁶Lawrence Livermore National Laboratory, Livermore, CA 94550, USA

⁷Laboratory for Laser Energetics, University of Rochester, Rochester, NY 14623, USA

(Received 14 October 2021; revised 8 March 2022; accepted 9 March 2022)

Following indirect-drive experiments which demonstrated promising performance for low convergence ratios (below 17), previous direct-drive simulations identified a fusion-relevant regime which is expected to be robust to hydrodynamic instability growth. This paper expands these results with simulated implosions at lower energies of 100 and 270 kJ, and ‘hydrodynamic equivalent’ capsules which demonstrate comparable convergence ratio, implosion velocity and in-flight aspect ratio without the need for cryogenic cooling, which would allow the assumptions of one-dimensional-like performance to be tested on current facilities. A range of techniques to improve performance within this regime are then investigated, including the use of two-colour and deep ultraviolet laser pulses. Finally, further simulations demonstrate that the deposition of electron energy into the hotspot of a low convergence ratio implosion through auxiliary heating also leads to significant increases in yield. Results include break even for 1.1 MJ of total energy input (including an estimated 370 kJ of short-pulse laser energy to produce electron beams for the auxiliary heating), but are found to be highly dependent upon the efficiency with which electron beams can be created and transported to the hotspot to drive the heating mechanism.

Key word: fusion plasma

† Email address for correspondence: robert.paddock@physics.ox.ac.uk

1. Introduction

The convergence ratio (CR) of a capsule, a measure of its total compression, defined in this paper by

$$CR = R_I/R_{HS}, \quad (1.1)$$

where R_I is the initial radius of the interior edge of the plastic capsule shell and R_{HS} is the hotspot radius at the time of maximum compression, is an important quantity in inertial confinement fusion (ICF) research. Increasing CR (in the absence of instabilities) leads to increased fusion yields, and as a result it is typical to aim for high CR values (the National Ignition Campaign (NIC) at the National Ignition Facility (NIF) targeted CR values in the range of $30 < CR < 40$ (Lindl *et al.* 2014), while current NIF implosions target CR values above 25 (Zylstra *et al.* 2021). However, implosions with high CR values are also susceptible to increased hydrodynamic instability growth (Smalyuk *et al.* 2020). These instabilities significantly degrade experimental performance, and overcoming them is one of the key barriers to achieving ignition.

Reducing the CR is widely known to reduce instability growth (Haines *et al.* 2019), and it has been observed numerous times that low-CR implosions demonstrate increased agreement with hydrodynamic simulations (see Nishimura 2000; Meyerhofer *et al.* 2001; Li *et al.* 2002; Lindl *et al.* 2004; Kato *et al.* 2008; Le Pape *et al.* 2014; Khan *et al.* 2016; Haines *et al.* 2017). This was demonstrated recently at the NIF by Olson *et al.* (2016) and Zylstra *et al.* (2018), where good agreement was observed between experiment and simulation with indirectly driven low-CR wetted-foam capsules. The use of wetted-foam layers is a significant advance, and allows unprecedented levels of control over CR by controlling the initial temperature of the capsule (Walters *et al.* 2018).

Following these results, a one-dimensional (1-D) simulation campaign was conducted by the authors of this paper (Paddock *et al.* 2021), which demonstrated that inertial fusion energy (IFE) relevant gains could potentially be achieved using the direct drive approach at low CR. In both that paper and this work gain is used as shorthand for ‘capsule gain’, and is calculated as the produced neutron energy divided by the total input energy (in most cases, the laser energy). As part of this work, a regime was defined based around limiting CR, implosion velocity, in-flight aspect ratio (IFAR) and applied laser intensity. Instability growth within this regime is expected to be low, and thus reasonable agreement between simulation and experiment is predicted.

Section 2 describes progress to enable experimental verification of the previous work. One aspect of this is the development of new implosions at 100 and 270 kJ of laser input energy, extending the work in Paddock *et al.* (2021) to lower energies available currently on both Laser Mégajoule (LMJ) and the NIF, and thus more suitable for experiments. In addition, one of the key limitations discussed in Paddock *et al.* (2021) was that the cryogenic temperatures required by the wetted-foam capsules are not currently compatible with the direct-drive configuration proposed, due to the lack of cryogenic direct-drive platforms at relevant facilities (Hohenberger *et al.* 2015). This is also addressed with the development of new ‘hydrodynamic equivalent’ capsules, which allow the regime described in Paddock *et al.* (2021) to be tested without the need for cryogenic cooling. These capsules therefore present designs that could potentially be tested experimentally on current facilities.

This work exists in the context of the recent result of a 1.3 MJ fusion yield at the NIF (Bishop 2021). This is an important milestone towards addressing the ‘grand challenges’ of ignition and IFE (Nuckolls 2010) and a significant achievement, and suggests that break even may be within reach in the near future. However, despite this success, there is still an important and urgent need for techniques to reduce the energy required to achieve ignition.

Tynan & Abdulla (2020) highlighted that the economics of a future low-carbon energy system would likely require that IFE reactors are small (of the order of 100 MW_e) in order to be economically viable. This will likely necessitate smaller facilities and low drive energies, highlighting the need for techniques to reduce the energy for ignition even in light of this recent result. Consequently, §§ 3 and 4 of this paper identify potential techniques that could hopefully soon be realised to enable increased fusion performance in the low instability regime at lower energies.

Following results from Obenschain *et al.* (2020) highlighting the increase in IFE performance that could be achieved by using argon fluoride (ArF) lasers, applied to shock ignition ICF, § 3 investigates performance in the low-instability regime when using higher frequency laser drivers. The optimisation process from Paddock *et al.* (2021) is repeated at the 193 nm ArF wavelength, to ascertain the potential benefits of moving to such a frequency (or similar high frequencies of Nd:glass lasers, such as the fifth harmonic at 210 nm). A new two-colour implosion scheme is then presented. In this two-colour approach, a series of initial pulses are applied by a conventional third-harmonic Nd:glass laser, followed by a later high-power laser pulse from an ArF laser. Such a sequence allows for thicker capsule shells and thus more fuel. This technique offers lower fusion performance than a 193 nm implosion, but requires significantly lower ArF laser energies (with the bulk of the laser energy being provided using conventional third-harmonic lasers – a mature technology).

Finally, § 4 simulates the performance that may be possible when combining implosions within this regime with auxiliary heating techniques. Electron energy is deposited into the hotspot around the bang time of the implosion, simulating the effect of a heating scheme proposed by Ratan *et al.* (2017) (following previous Vlasov–Maxwell simulations performed by Norreys *et al.* 2021). Auxiliary heating schemes are an area of active research and continue to develop (with, for example, recent demonstrations of channel formation in plasmas confirming the feasibility of electron beam propagation through such a capsule by Ceurvorst *et al.* 2016; Spiers *et al.* 2021), and could potentially play a key role in developing IFE (Norreys 2021). The encouraging results discussed in § 4, along with similar results previously shown for indirect-drive implosions by Norreys *et al.* (2021), provide further evidence of the promise of such an approach.

1.1. Burning plasma parameter

Throughout this paper, the ‘burning plasma parameter’, Q_{α}^{tot} , is used alongside gain as a metric of capsule performance. A number of variations of this parameter exist, but the version used in this work, the ‘total capsule burning plasma parameter’, is defined as

$$Q_{\alpha}^{\text{tot}} = \frac{1}{2} \frac{E_{\alpha}}{E_{\text{PdV}}^{\text{tot}}}, \quad (1.2)$$

where E_{α} is the alpha particle energy deposited back into the hotspot over the total duration of the implosion, and $E_{\text{PdV}}^{\text{tot}}$ is the total work done on the capsule hotspot and shell at the time of stagnation (maximum pressure) (Betti *et al.* 2015). The factor $\frac{1}{2}$ is used to approximate the absorbed alpha energy up to the bang time; it is assumed that the thermonuclear burn is roughly symmetric in time around this point, and thus that the alpha energy absorbed up to the bang time is roughly half of that absorbed over the whole implosion, E_{α} . Therefore, Q_{α}^{tot} compares the energy absorbed by the hotspot from alpha particles generated in the fusion reactions (the alpha self-heating of the hotspot) up to the bang time, with the external energy used to compress and heat the capsule.

A value of $Q_{\alpha}^{\text{tot}} > 1$ therefore means that alpha heating is the dominant source of energy and is used to define the ‘burning plasma’ regime – a key milestone on the path to IFE (Christopherson *et al.* 2020). It is important to note that this quantity is distinct from the ‘hotspot burning plasma parameter’ Q_{α}^{hs} , which replaces $E_{\text{PdV}}^{\text{tot}}$ instead with the total work done on the hotspot only (i.e. neglecting work done on the shell), and is thus typically twice as large (Betti *et al.* 2015). A rough estimate of the ignition threshold can also be set as $Q_{\alpha}^{\text{tot}} = 10$, when the cumulative alpha heating at the bang time is ten times greater than the work done on the hot spot and shell (Betti 2011). However, the exact meaning of ‘ignition’ is not widely agreed and this definition is not a commonly used one, so it is used here only to give an estimate of progress rather than as a strict threshold.

The burning plasma parameter is a particularly useful metric for the auxiliary heating simulations discussed in § 4. Whereas gain (which is a more conventional metric for IFE applications) can change dramatically depending on the efficiency with which the heating energy can be delivered (such as how efficiently electron beams can be produced), the burning plasma parameter depends only on the energetics of the implosion itself. This makes it far more robust for measuring capsule performance in cases such as this, where these up-stream efficiencies are not known with high certainty.

2. Experiment-ready low-instability implosions

2.1. Reduced energy implosions

The lowest-energy capsule considered in Paddock *et al.* (2021) required a laser energy of 0.8 MJ, which is towards the upper end of energies available on current facilities. It is therefore desirable to reduce this energy. Doing so would make the capsule more favourable for initial proof-of-concept experiments, avoiding some of the difficulties associated with higher-energy experiments. It is also interesting to see how the performance scales to smaller capsule radii.

As such, two lower-energy capsules were designed and simulated using HYADES, following the process described in Paddock *et al.* (2021). For the first of these capsules, a sub-300 kJ laser input energy was designed in order to be compatible with the current laser energies available on LMJ (in order to produce a capsule that could be tested on either that facility or the NIF). Because laser power is set by the capsule size and laser pulse timings are varied in the optimisation, the laser energy is not finalised until the process is complete. The resulting optimised implosions are described in table 1. A new high-energy implosion at 2.8 MJ is also included, which was designed to add another data point in the large gap between the 1.7 and 4.2 MJ implosions presented in Paddock *et al.* (2021). In order to reduce the number of simulations required, the 1.7 MJ implosion was first scaled to this energy using the hydrodynamic scaling relations $t, R \propto E^{1/3}$, where t and R , are the implosion timings (including all laser timings) and capsule radii (including all internal boundaries) respectively, and E is the laser energy (Nora *et al.* 2014). This scaled capsule already had a good level of performance, and was then used as the starting point for the optimisation procedure – significantly reducing the time and number of simulations required to achieve the presented level of performance.

The conditions achieved in the shell and hotspot for the ‘270 kJ’ capsule can be seen in figure 1, while the capsule structure and laser pulse sequence can be seen in figures 2 and 3, respectively. As expected, the temperatures and areal densities achieved within the hotspot and shell are considerably lower for the new low-energy wetted foam capsules than for the previously presented implosions. In this paper, areal density is defined as the integral of density against radius over the region of interest. This sums linearly, so that the combined areal density of the shell and hotspot is the sum of the areal densities in these two regions

Capsule label	A	B	—	C	D	—
Capsule name	100 kJ	270 kJ	270 kJ H.E.	0.8 MJ	1.7 MJ	2.8 MJ
Laser energy (kJ)	101	270	244	768	1710	2780
Gain	0.030	0.067	0.0094	0.19	0.75	6.1
Convergence ratio	15.7	15.7	16.0	16.0	15.8	16.0
IFAR	23.4	27.5	28.4	29.7	25.1	23.8
Implosion velocity (km s ⁻¹)	391.4	395.8	396.3	399.6	399.6	387.8
Max pulse power (TW)	43.26	84.79	84.79	173.00	292.38	389.36
Pulse 2 switch on time (ns)	1.10	2.20	2.70	2.60	3.60	4.20
Pulse 3 switch on time (ns)	3.00	4.60	4.90	5.60	7.80	8.80
Pulse 4 switch on time (ns)	3.60	5.50	5.80	6.80	9.50	10.90
Laser switch off time (ns)	5.80	8.50	8.50	11.00	15.00	17.65
Vapour/liquid boundary (mm)	0.6325	0.8950	0.9050	1.3050	1.6705	1.9275
Liquid/CD boundary (mm)	0.69625	0.976	0.980	1.3950	1.8200	2.1000
Outer radius (mm)	0.7125	0.9975	0.9975	1.4250	1.8525	2.1375
Vapour density (mg cm ⁻³)	1.35	1.35	4.00	1.05	1.00	0.90

TABLE 1. Simulation parameters for the two new low-energy wetted-foam implosions, one new hydrodynamic equivalent (H.E.) capsule and the new 2.8 MJ wetted-foam implosion. The 0.8 and 1.7 MJ capsules from Paddock (2021) are included for reference. The capsule labels A–D refer to labels used in § 4. Gain is used here to refer to ‘capsule gain’, calculated as the neutron energy emitted divided by the input laser energy.

individually. This is contrary to the definition used previously in Paddock *et al.* (2021), where the areal density of the target was taken as a mass average over the region of interest for the product of density and radius in each zone. The methodology used here produces a reduced average value for the total capsule areal density than that used previously. On the other hand, the areal density calculated for the hotspot (such as that seen in figure 5 of the previous work) is similar for the two approaches. A second implosion at a further lower energy, the ‘100 kJ’ implosion, was also designed and is included in table 1.

These designs provide implosions within the low-instability regime at more favourable energy scales for experimental work, and at energies compatible with existing facilities. However, because experiments using this approach are currently precluded by the lack of suitable cryogenic platforms, room temperature ‘hydrodynamic equivalent’ capsules have been developed.

2.2. Hydrodynamic equivalent capsules

The wetted-foam capsules presented in § 2.1 and in Paddock *et al.* (2021) consist of three layers: a central void containing deuterium-tritium (DT) vapour, a deuterated plastic foam wetted with liquid DT and a deuterated plastic shell. In order to enable implosions within this low-instability regime at room temperatures, new ‘hydrodynamic equivalent’ capsules replace the wetted-foam layer with a higher density non-wetted foam (containing no DT in the foam layer). The structure of the 270 kJ wetted-foam capsule and its hydrodynamic equivalent can be seen in figure 2 (while the laser pulse sequence for the two capsules is displayed in figure 3). In the original capsule, the wetted-foam layer consisted of a low density foam (~ 25 mg cm⁻³) saturated with liquid DT, giving an overall layer density of 0.253 g cm⁻³. In the new capsule this layer is replaced with a higher density 0.253 g cm⁻³ foam, without any DT, to leave the overall layer density unchanged. Other than the density

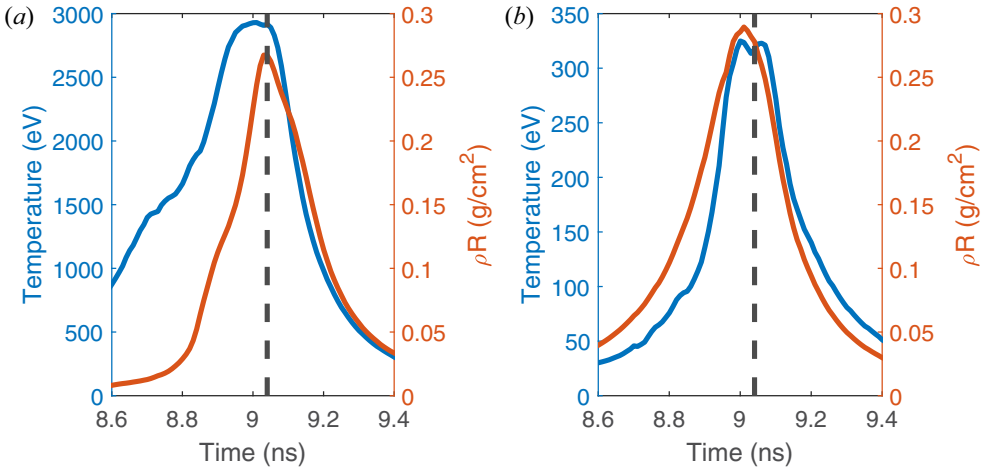


FIGURE 1. Areal density and ion temperature within the hot spot (a) and shell (b) for a wetted-foam 270 kJ implosion in the low-instability regime, produced following the optimisation process described in Paddock *et al.* (2021). The dashed black line represents the bang time (time of maximum neutron generation).

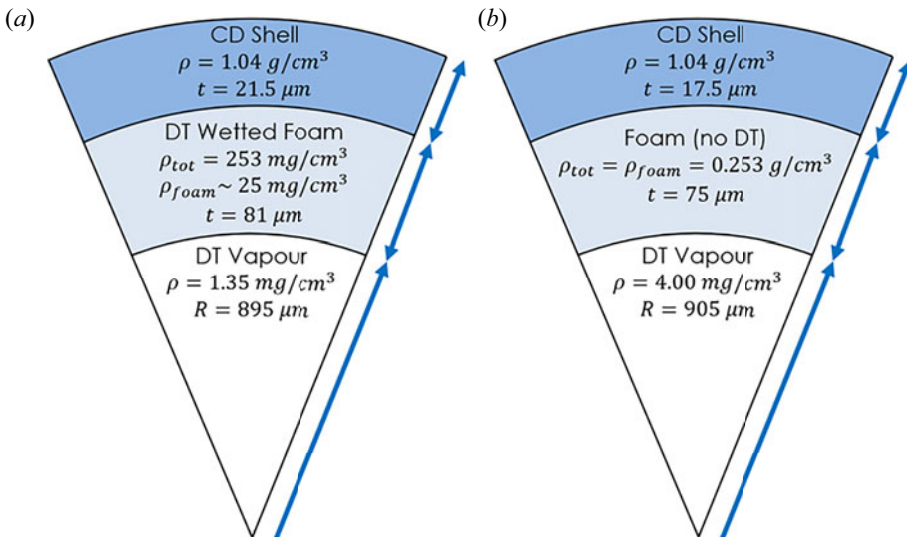


FIGURE 2. The structure of the 270 kJ wetted-foam capsule (a) and the 270 kJ hydrodynamic equivalent capsule (b). The hydrodynamic equivalent capsule uses a higher density foam than the original capsule, so that the density of the layer remains the same even though there is no longer any DT present. The dimensions of the layers (and the vapour density) have also been adjusted to re-optimize the capsule.

and presence/absence of DT, the foam used in the two capsules is equivalent. The 270 kJ hydrodynamic capsule of table 1, along with hydrodynamic equivalent versions of the 0.8 and 1.7 MJ capsules of Paddock *et al.* (2021), were simulated using the 1-D radiation hydrodynamics code HYADES (Larsen & Lane 1994).

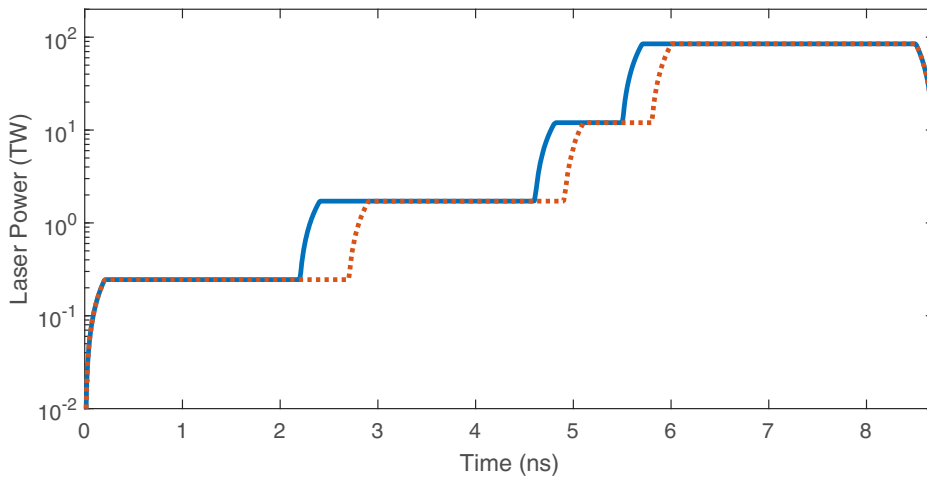


FIGURE 3. Temporal laser profile for the 270 kJ wetted-foam (solid blue line) and hydrodynamic equivalent (dashed orange line) implosions. The same pulse powers are used in both (0.245, 1.715, 12.01 and 84.79 TW), but the optimisation process results in these pulses being applied at different times.

The details of the 270 kJ hydrodynamic equivalent capsule are included in [table 1](#). Replacing the wetted-foam layer has a significant impact on the fusion yield, as a large proportion of the DT fuel has been removed from the capsule. However, the hydrodynamic behaviour of the capsule is relatively similar, as the layer densities have remained constant. After some re-optimising of the thicknesses of the different layers (while keeping the overall capsule radius constant), the laser timings and the vapour density (as in the optimisation presented in [Paddock *et al.* 2021](#)) were obtained and similar values for CR, implosion velocity and IFAR to the original wetted-foam implosion were found. These hydrodynamic equivalent implosions therefore also satisfy the four criteria for low-instability growth identified in [Paddock *et al.* \(2021\)](#), and thus 1-D-like performance is again expected.

The hydrodynamic equivalent capsules therefore provide a potential route towards experimental verification of this low-instability regime. As they do not require cryogenic cooling, they can be tested on current experimental facilities (in a polar direct-drive configuration ([Skupsky *et al.* 2004](#))). The experimental performance can then be compared with the simulated results, and the level of agreement between experiment and simulation in this regime quantified. If this agreement is high (the assumption upon which the work in [Paddock *et al.* \(2021\)](#) was based), then this likely means that the criteria used for CR, implosion velocity, IFAR and laser intensity are sufficient to ensure low-instability growth, and thus that the higher gain results presented in [Paddock *et al.* \(2021\)](#) are also likely accurate.

These capsules can also be adjusted for compatibility with additional requirements that experimental facilities may have. For instance, it is possible to adapt the capsule to operate using pure deuterium vapour in the place of pure DT (which has been required on recent LMJ experiments). For the 270 kJ hydrodynamic equivalent capsule, substituting the DT vapour for deuterium requires no further changes to the capsule than re-optimising the vapour density until equivalent performance was obtained (found to be at 3.45 mg cm^{-3}). While the gain is significantly reduced (to 6.9×10^{-5}), the key quantities of CR (15.9), IFAR (28.2) and implosion velocity (399.9 km s^{-1}) are largely similar. This highlights

the flexibility of this new technique, and further demonstrates how the use of such hydrodynamic equivalent capsules can allow experiments to verify the low-instability regime identified in Paddock *et al.* (2021) under a wider range of experimental constraints.

3. High frequency and two-colour implosions

3.1. High frequency (193 nm) implosions

Performing implosions at higher laser frequencies offers a range of potential advantages. Firstly, higher frequency lasers have an increased energy coupling with the plasma, resulting in higher ablation pressures for the same laser intensity, I . The higher frequency laser has a higher critical density and thus propagates further into the plasma, resulting in more laser absorption and a higher density blow-off (Obenschain *et al.* 2020). Furthermore, the lower wavelength permits higher laser intensities before the onset of parametric instabilities (Montgomery 2016), enabling higher laser powers to be used for equivalent instability growth.

Recent simulation work by Obenschain *et al.* (2020) demonstrated that significant gains can be achieved at low laser energy using wavelength $\lambda = 193$ nm ArF laser drivers when applied to shock ignition, leading the authors to highlight the potential role of such lasers for IFE applications. In order to investigate these advantages further the optimisation process performed in Paddock *et al.* (2021) was repeated, but the laser wavelength specified in the simulation was set to 193 nm rather than the third-harmonic wavelength previously used. The power of the applied laser pulse sequence was scaled with the inverse of wavelength squared, in order to maintain a constant $I\lambda^2$ for the implosion as in Paddock *et al.* (2021). The intensity for this purpose was calculated using the maximum laser power and the initial capsule radius.

Other than this change to maximum intensity, and the change to the laser frequency (which in HYADES requires only a change of the wavelength parameter in the input deck), the nature of the implosion is unchanged from those described in § 2.1 and Paddock (2021). The wetted-foam capsule consists of the same structure and composition, and a four-pulse laser sequence is still used. The same parameters (internal capsule layer thicknesses, laser pulse timings and DT vapour pressure) are again optimised, following the exact procedure described in the previous work. This is one of the advantages of this optimisation campaign – it is easily repeated to investigate similar implosions in a different region of parameter space (in this case, using the higher frequency). The four criteria used in Paddock *et al.* (2021) to satisfy the low instability regime were again satisfied, again suggesting that instability growth should be minimal and the 1-D simulated results should provide a reasonable estimate of performance. These results obviously are directly relevant for potential future ArF facilities, but similar performance would be expected for similar high frequencies (such as fifth harmonic Nd:glass lasers).

For a given capsule radius, using a higher frequency laser resulted in a larger implosion energy. The higher power and increased coupling would lead to a larger implosion velocity for a given shell thickness, but in this work the implosion velocity is limited to 400 km s^{-1} . As such, changes to the capsule/implosions (such as increasing the thickness of the shell) must be made to keep the implosion velocity below this value. This results in an implosion with higher power applied over a similar implosion time (since the implosion velocity has remained constant), resulting in a larger total energy. Of course, this also corresponds to a significantly higher yield/gain. The parameters used to achieve the best results for three different capsule sizes are given in table 2. The larger shell is reflected in the low IFAR values for these implosions. The performance of these capsules will be discussed in § 3.3.

Implosion Type	ArF			Two-colour			
Total laser energy (MJ)	1.59	1.91	4.55	1.69	2.10	3.12	4.27
Third-harmonic energy (MJ)	—	—	—	0.92	1.82	2.75	3.96
ArF energy (MJ)	1.59	1.91	4.55	0.77	0.28	0.37	0.32
Gain	10.9	17.3	34.5	4.0	15.5	20.4	30.5
Convergence ratio	16.0	15.9	14.0	16.0	16.0	16.0	16.0
IFAR	11.3	10.5	8.5	16.1	20.4	23.8	23.4
Implosion velocity (km s^{-1})	390.7	398.9	360	391.1	399.9	396.4	391.6
Max third-harmonic power (TW)	—	—	—	173	292	389	500
Max ArF laser power (TW)	464	572	967	274	463	617	792
Pulse 2 switch on time (ns)	3.90	3.50	2.50	1.95	3.00	2.70	3.50
Pulse 3 switch on time (ns)	7.10	7.50	8.90	4.35	7.80	7.20	9.10
Pulse 4 switch on time (ns)	8.85	9.25	10.80	8.05	9.40	9.10	11.10
2nd laser switch on time (ns)	—	—	—	10.00	14.70	15.20	18.20
Laser switch off time (ns)	11.95	12.25	15.10	12.80	15.30	15.80	18.60
Vapour/ice boundary (mm)	1.072	1.210	1.435	1.230	1.645	1.933	2.210
Ice/CD boundary (mm)	1.200	1.340	1.780	1.360	1.818	2.100	2.374
Outer radius (mm)	1.2800	1.425	1.8525	1.425	1.8525	2.1375	2.4225
Vapour density (mg cm^{-3})	1.00	1.03	0.60	1.02	1.05	1.00	1.01

TABLE 2. Simulation parameters for the two-colour and high frequency implosions.

3.2. Two-colour implosions

ArF laser technology is significantly less developed than Nd:glass, and the high laser energies presented in § 3.1 would therefore be very challenging to achieve in practice. As such, an alternate scheme is proposed where ArF lasers are used to supplement a third-harmonic driven implosion. While the ArF laser energy requirements of such a scheme are still large compared with the current standard, they are a significant reduction compared with the energies discussed in § 3.1. This technique will be referred to as ‘two colour’, in reference to the two frequencies involved. A four-pulse third-harmonic sequence (with a time profile of the form seen in figure 3) is first applied to a capsule. Then at a late stage in the implosion, a high-power pulse of shorter duration is applied. While the four-pulse sequence is already at the $I\lambda^2$ threshold, using a lower wavelength for the late pulse enables a further increase in power. The use of multiple frequencies has been demonstrated to reduce parametric instability growth (Follett *et al.* 2018), and thus the $I\lambda^2$ condition is applied here separately for the two laser colours, given the large difference in frequency between them. The other criteria from Paddock *et al.* (2021) continue to be applied, meaning (amongst other conditions) that the implosion velocity is at no point allowed to increase past 400 km s^{-1} . Heavier shells are therefore used which are accelerated to lower initial velocities, with the ArF pulse then further accelerating them closer to the 400 km s^{-1} limit. An example laser profile can be seen in figure 4.

Applying two laser colours in this way has a variety of advantages. The bulk of the laser energy is delivered by a third-harmonic Nd:glass laser system – a mature technology that can already produce the energies required. The benefits of higher frequency lasers (particularly the ability to use higher intensities while continuing to minimise parametric instability growth) can be captured, but for significantly lower required amounts of laser energy. Finally, the two-laser concept makes it a natural fit for the ‘zoomed focus’ technique (Kehne *et al.* 2013; Eimerl *et al.* 2014). In a standard implosion the laser

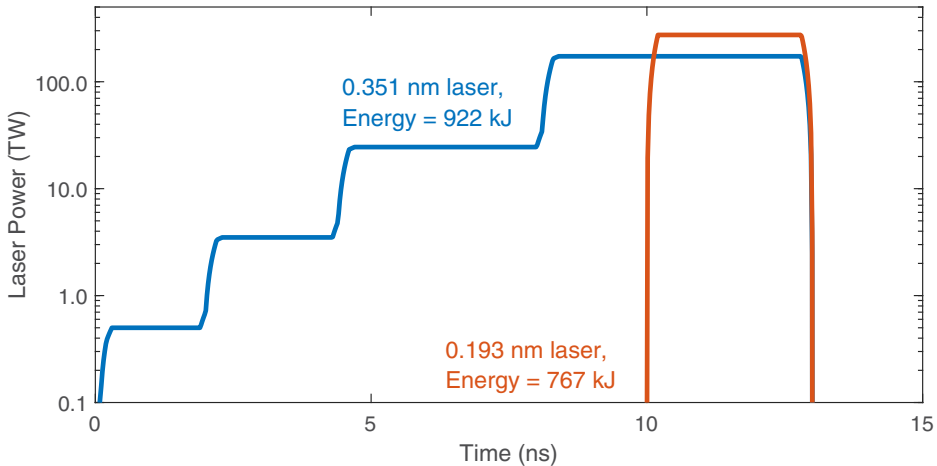


FIGURE 4. Temporal laser profile for the 1.69 MJ two-colour implosion. A four-pulse third-harmonic pulse sequence is applied, with a final high-power ArF frequency pulse applied late in the implosion. These two frequencies are applied concurrently, until they are both switched off at the same time.

is focused on the initial capsule radius, resulting in increased losses as the capsule radius decreases throughout the experiment. The concept of the zoomed focus has been demonstrated experimentally on the Nike laser, where the focus of the laser was changed to a smaller radius part way through the implosion to reduce these losses (Kehne *et al.* 2013). The two-colour approach suggested here is a natural fit for such an approach, as the second (high frequency) laser pulse (which is applied late in the implosion to an already compressed capsule) could be focused at a smaller capsule radius than the original laser pulse. This would capture the benefits of the zoomed focus technique, without needing to change the focus of any given laser beam during the pulse. These losses (and thus the benefit of the zoomed focus technique) are not observed in the 1-D HYADES simulations, however, as the laser beams remain perfectly focused on the centre of the capsule for all radii.

The structure and composition of the capsule and the nature of the four-pulse third-harmonic pulse sequence are again unchanged from Paddock *et al.* (2021). The addition of an extra laser pulse (at the higher frequency and higher intensity) adds an additional optimisation parameter, in the time that the new pulse is applied. The optimisation procedure (and criteria to be satisfied) are again unchanged, allowing the effect of the two-colour implosion to be investigated with minimal additional work.

Table 2 shows the best achieved results within this regime for three different capsule sizes. The larger laser powers again lead to thicker shells (i.e. thicker foam and ablator regions), which in turn lead to lower IFAR values. This makes the capsule more robust against Rayleigh-Taylor (RT) instability growth. However, it is worth noting the difficulty in applying conventional RT growth rate equations to two-colour implosions. IFAR is a continually evolving variable, but by convention the single IFAR value quoted is that calculated when the capsule shell is at two thirds of the initial capsule radius. The RT growth rate equations in Paddock *et al.* (2021) make some basic assumptions about the form of the implosion, and can thus use this single IFAR value to estimate instability growth. However, the time at which this value is recorded is before the second laser is applied, and so the effect of this high-power pulse is not included in this value. Such pulses

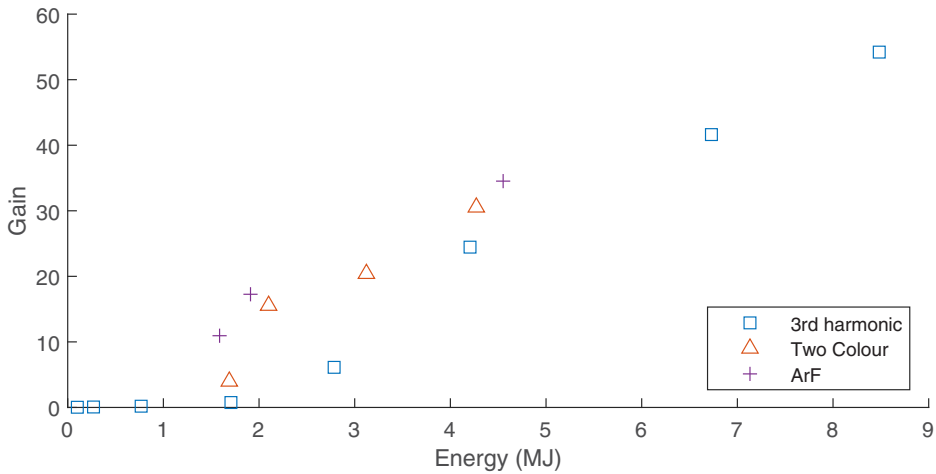


FIGURE 5. Gain for the third-harmonic (blue squares), two-colour (orange triangles) and ArF implosions (purple pluses) against total laser energy (including both third-harmonic and ArF lasers in the case of the two-colour results).

are a significant deviation from the assumptions the RT growth equations make on how the implosion will develop, and it is thus not guaranteed that the IFAR values described here can be used with such equations. Given that (a) these IFAR values are low even compared with our restrictive upper limit of 30; (b) additional measures have been taken to minimise instability growth; and (c) the additional pulse is applied late in the implosion (so any higher growth rate will have a much reduced time over which it is applied), it is expected that these implosions will still have low-instability growth. However, this highlights the need for further study of such implosions, particularly simulations in higher dimensions where RT growth can be measured.

3.3. Discussion

The gains of the third harmonic, ArF and two-colour implosions have been calculated, and are displayed in figure 5. For a given laser energy the ArF implosions offer the highest gains, with a substantial increase over the third-harmonic implosions. A gain of 11 is achieved for around 1.6 MJ of total energy, an order of magnitude higher than predicted for third-harmonic light. The two-colour implosions offer a reduced, but still substantial, improvement compared with operating at the third harmonic. This approach shows a gain of 4 for 1.7 MJ of total energy, around half that of the ArF result, but still five times greater than the third-harmonic implosion (and significantly above breakeven for under 2 MJ). As can be seen in table 2, the two-colour implosions have significantly lower ArF energies than the single-colour ArF implosions. Increasing the energy to 2.1 MJ sees the the gain of the two-colour implosions increase to 15.5, while requiring less than 300 kJ of ArF energy. This approach therefore offers a way to benefit from the increased performance available with ArF, but using far more modest high frequency laser energies (although such an approach would require a facility supporting two laser systems).

There is an additional expected benefit associated with operating the second laser with a smaller focal spot. While this could not be simulated here, it could result in the two-colour performance being closer to that of the ArF implosions. It can be seen that there is significant variation in the proportion of energy provided by the ArF pulse,

highlighting that further increased performance may still be possible in this regime (this is a reflection of the increased number of variables to optimise over, making a more thorough optimisation difficult to achieve). These results are intended simply as a first estimate of the level of performance available using this approach, but the increase in gain from the previous third-harmonic simulations demonstrates clearly the potential of this technique. Considering also the single-colour ArF implosions, these results provide significant support for the claims made in previous works about the benefits that operating at higher frequencies could offer IFE research.

The burning plasma parameter Q_{α}^{tot} has also been calculated for each of these implosions. Some approximations were required for the variables in (1.2), to reduce dependence on hotspot tracking (as the definition of hotspot used, given in Paddock *et al.* (2021), showed some variation throughout the latter stages of the implosion). The total work done on the capsule, $E_{\text{pdv}}^{\text{tot}}$, was taken as the sum of kinetic and thermal energy within the hotspot and shell. This energy was measured at the point when the thermal and kinetic energy of the capsule are equal (during the deceleration of the shell, as the hotspot temperature begins to rise). This gave a robust measurement of the total energy before fusion begins to occur, at a time when the total energy is relatively constant (this behaviour is visible in figure 8 in § 4.1, which discusses the energetics of these implosions around the bang time in more detail). In addition, the deposited alpha energy over the full capsule (rather than just the hotspot) was used as an estimate of E_{α} . It is expected that this absorption is dominated by the hotspot (Christopherson *et al.* 2018), and thus that this is a reasonable approximation.

It is clear from figure 6 that all of the two-colour and ArF implosions simulated are well above the burning plasma threshold, and all but one (the lowest-energy two-colour implosion) are above the $Q_{\alpha}^{\text{tot}} > 10$ approximate ignition threshold. Using this threshold suggests that ignition occurs in this regime for significantly below 2 MJ for the ArF implosions, at around 2 MJ for two-colour implosions and at around 3 MJ for third-harmonic implosions. It is also clear that the 1.7 MJ third-harmonic implosion from Paddock *et al.* (2021) is above the burning plasma threshold, again confirming the promise of this result. The prospect of ignition at sub-2 MJ energies again highlights the potential of higher frequency IFE research.

4. Auxiliary heating

In Paddock *et al.* (2021), it was noted that the areal density of the hotspot achieved by the 0.8 MJ capsule exceeded 0.3 g cm^{-2} , which is considered sufficient for ignition (Lindl 1995). However, the ion temperature of around 3.5 keV that accompanied this was too low for ignition to occur (Cheng *et al.* 2021). It was suggested that such implosions would therefore be promising candidates for auxiliary heating schemes, where additional mechanisms are used to increase the temperature around the time of maximum compression. Such a scheme was described by Ratan *et al.* (2017), who proposed crossing two relativistic electron beams inside the hotspot of an implosion. This method requires a large hotspot, making it a natural fit with the low CR approach suggested here. This approach is distinct from fast ignition due to the use of a conventional isobaric central hotspot implosion before the addition of the electron energy, rather than an isochoric implosion (Atzeni & Meyer-ter Vehn 2008). The fact that the energy is transferred at the overlap of the two beams also means that the heating can be performed in the centre of the capsule (unlike in fast ignition where the hotspot typically forms on one side of the fuel, leading to greater energy losses). It could also be possible to use alternative methods, such as shock ignition, to improve the performance of these low-instability implosions. However, shock ignition requires much higher intensities to generate the large final shock,

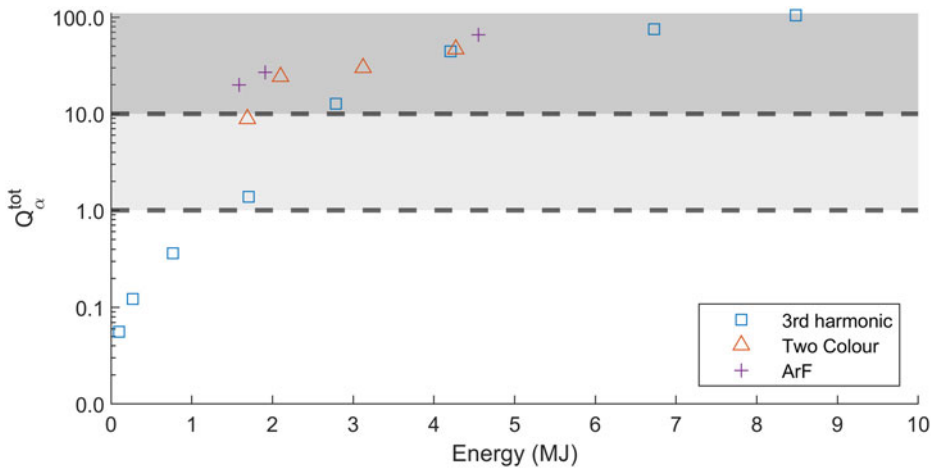


FIGURE 6. Approximate total capsule burning plasma parameter vs total laser energy for the third-harmonic (blue squares), two-colour (orange triangles) and ArF implosions (purple pluses). The lightly shaded region above $Q_{\alpha}^{\text{tot}} = 1$ represents the burning plasma regime, where the energy deposited by the alpha particles up to the bang time exceeds the hydrodynamic assembly energy of the capsule, while the darker shaded region indicates a rough threshold for ignition of $Q_{\alpha}^{\text{tot}} > 10$.

and these would not be permitted under the $I\lambda^2$ restriction of the low-instability regime. As such, this idea is not explored in this paper.

Simulating such a heating scheme is difficult, due to the nature of the simulation codes available. In order to simulate a full ICF implosion, radiation hydrodynamic codes which can simulate time scales over tens of nanoseconds are normally used. However, such codes are incapable of simulating the mechanism for the auxiliary heating seen here due to the disparate length and time scales involved (where overlapping electron beams drive Langmuir waves in the plasma, and electron–ion collisions equilibrate this additional energy into the ions over a time scale of a few picoseconds). In order to investigate such a scheme, it is therefore necessary to use different types of simulation code to calculate the heating process separately, and to somehow include these results into a radiation hydrodynamic simulation to determine the effect it would have on the overall implosion. Vlasov–Maxwell simulations performed by Ratan *et al.* (2017) investigated the interaction between overlapping electron beams and a relevant plasma, demonstrating that such a heating scheme does in fact drive an increase in electron temperature (and subsequently ion temperature), with an estimated coupling efficiency between the beam energy and the electrons in the background plasma of around 18%. This was simulated for a head-on interaction between the two beams, although it is expected that alternative (such as orthogonal) configurations may increase this efficiency further.

This paper builds upon this work by performing 1-D radiation hydrodynamics simulations in HYADES, to estimate the effect of such a scheme on a selection of capsules from § 2.1 and Paddock *et al.* (2021). The heating mechanism was not simulated – rather, electron energy was added artificially to the DT vapour regions at the centre of the capsule, over a total period of 0.7 ps (constant heating for 0.5 ps, with a 0.1 ps linear ramp on either side). This allows the effects of the auxiliary heating observed in the Vlasov–Maxwell simulation to be roughly approximated in the hydrodynamic simulation, thus allowing

the effect of such a scheme on the fusion performance of low-CR conventional hotspot implosions to be roughly approximated.

The conversion efficiency between electron beams and hotspot estimated by the Vlasov–Maxwell simulations suggests that the energy of the electron beams required to cause such heating would need to be roughly five times greater than the deposited electron energy in these simulations. It is notable that this value of 18 % is significantly greater than typical hydrodynamic efficiencies for energy transfer between the laser input and the hotspot (Campbell *et al.* 2017), which highlights how using auxiliary heating may offer advantages over using lasers alone (although the efficiency of creating the electron beam must also be considered). This is considered in § 4.4, where estimates are provided of the energy required for such a heating scheme to be implemented, and thus the gain that would be achieved.

The electron heating was simulated for four different implosions: the 100 and 270 kJ targets discussed in § 2.1, and the 0.8 and 1.7 MJ capsules presented in Paddock *et al.* (2021). Full descriptions of each implosion are given in table 1. For the purposes of clarity, these capsules/implosions will be referred to as A–D, in order of increasing energy. The applied laser energy in the simulations was not changed (i.e. simulations of capsule A always used the laser settings described in § 2.1 and thus 100 kJ of applied ‘long-pulse’ laser energy, regardless of the electron energy deposited). The two lowest energy capsules can also be compared with previous simulations of this approach for the NIF shot 160421 presented in Norreys *et al.* (2021). This implosion was a wetted-foam capsule with low convergence ratio and a similar structure to the capsules simulated here, but was shot in an indirect-drive configuration with a drive energy of ~ 800 kJ. Indirectly driven capsules typically have a coupling efficiency of approximately 1 % (Campbell *et al.* 2017), which corresponds to approximately 8 kJ of energy being inserted into the hotspot. Direct-drive implosions have higher efficiency, and typically lead to ~ 5 times more energy being deposited in the hotspot (Goncharov *et al.* 2016; Campbell *et al.* 2017). This suggests that the indirect-drive capsule in Norreys (2021) would correspond to a direct-drive energy of around 150 kJ, which fits between the two low-energy capsules considered in this work.

The ‘short-pulse’ laser energies required to produce the necessary electron beams for the heating discussed in this section are significantly higher than those available at current facilities. In fact, these energies are more comparable to estimates of the short-pulse energy necessary for fast ignition schemes (Strozzi *et al.* 2012). However, recent developments in the field of plasma beam combiners (Kirkwood *et al.* 2018a, 2018b) offer a potential opportunity for significant increases in laser energies compared with current technologies. Plasma beam combiners are plasma-based optical components which use nonlinear scattering interactions between multiple input beams to produce a single laser output with a much higher intensity than possible using conventional optics. This is an exciting area of research, and one which creates a pathway for the laser energies described in this work to be potentially realised in the near future (R.K. Kirkwood, personal communication 2021). It is therefore hoped that, while the high short-pulse energies are currently a barrier to this technique, developments in the field may soon address this concern.

4.1. Timing of electron deposition

Figure 7 displays the relative yield amplification caused by the deposition of 4 kJ of electron energy in each of the four capsules, for a range of deposition times around the bang times of the capsules without auxiliary heating. In this paper, relative yield amplification is used to mean the fusion yield produced when auxiliary heating is applied compared with the yield in the absence of auxiliary heating (rather than comparing the yield when alpha self-heating is and is not included, as it is often used). It is clear that

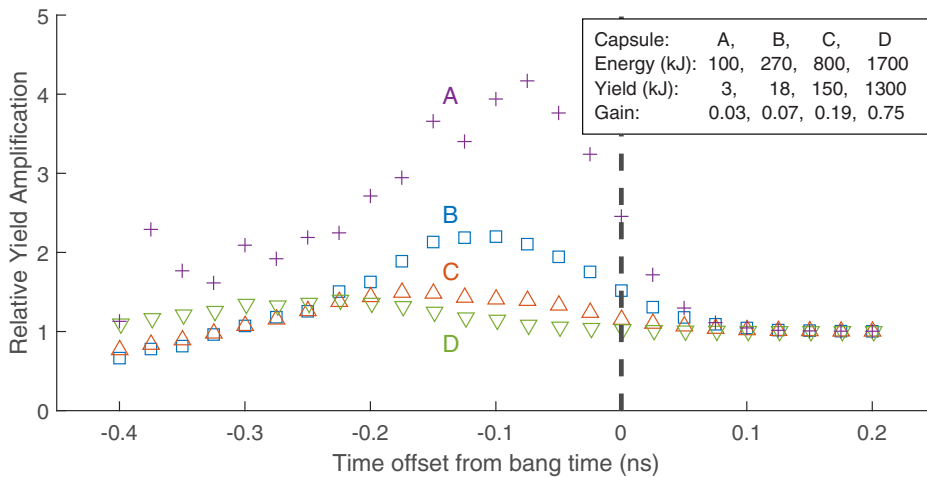


FIGURE 7. Relative yield amplification (compared with the capsules without auxiliary heating) for capsules A (purple pluses), B (blue squares), C (orange upward triangles) and D (green downward triangles) for 4 kJ of deposited electron energy. The electron energy deposition occurred over 0.7 ps, and the time at which this began was varied relative to the bang time as shown. The data for the 100 kJ capsule show significantly more variation than the others, likely due to the lower yield of this implosion. The table indicates the laser energy, yield and gain for each capsule in the absence of auxiliary heating.

there is an optimal window for heating to be applied for each capsule, and that this window is earlier for larger capsule sizes. Additional simulations looking at yield amplification vs deposition time for 20 kJ of deposited energy gave comparable optimal timings, suggesting that these timings are independent of the amount of deposited energy.

Figure 8 shows the distribution of thermal, kinetic and total energy within capsule B over this period, for both the capsule without auxiliary heating and for 20 kJ of deposited electron energy. The total energy is initially flat (as expected), with the kinetic energy being converted into thermal energy as the shell decelerates and the hotspot begins to heat up. Shortly after this time the thermal energy and total energy begin to increase, as fusion begins and energy feeds back into the system through alpha heating. The optimal time for electron energy deposition (determined from figure 7) occurs just before the minimum in kinetic energy (when the shell comes to a halt), and before significant fusion begins to occur. This was found to be the case for each of the four capsules. This makes intuitive sense as adding the energy to the hotspot before this point will make it harder to compress, disrupting the implosion and reducing the density, while adding it later (once significant amounts of fusion has occurred) means the deposited electron energy is lower relative to the total energy of the system (and occurs once the burn has already started, so has less of an effect). In the case when the electron energy is deposited, a sudden increase in the thermal and total energies of 20 kJ is observed (corresponding to the injected energy). The following increase in total energy due to alpha self-heating is then much more significant than in the case without auxiliary heating, corresponding to an increased number of fusion reactions.

4.2. Magnitude of deposited energy

Further simulations were then performed to investigate the effect of changing the amount of deposited electron energy. The energy was deposited at the optimal time for each

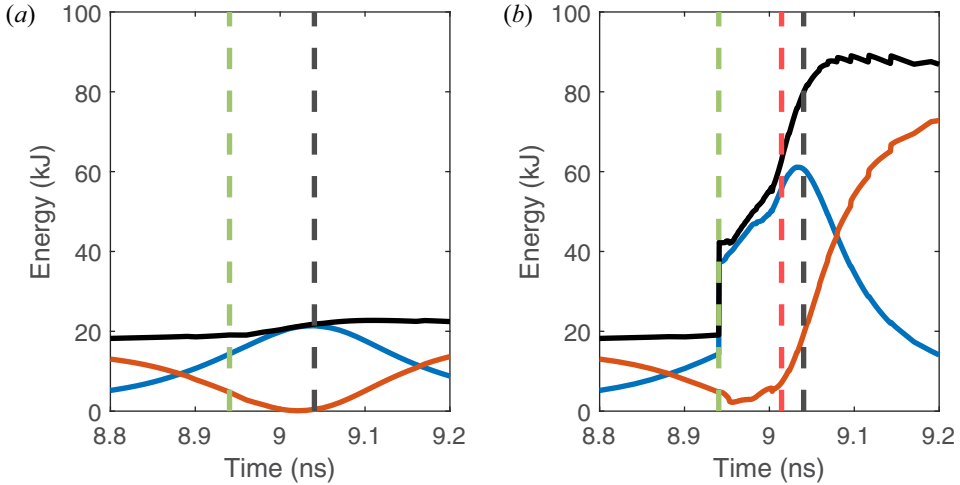


FIGURE 8. Combined total (black), thermal (blue) and kinetic (orange) energy for the shell and hotspot for capsule B. The left plot shows this breakdown for the capsule without auxiliary heating, while the right plot includes 20 kJ of deposited energy. The dashed lines represent the bang time of the capsule without auxiliary heating (black), the bang time of the heated capsule (red) and the optimal time for the deposition of electron energy (green).

capsule, as determined from figure 7. The results can be seen in figure 9. It is clear that adding modest amounts of electron energy can significantly amplify the yield. The relative amplification increases with decreasing capsule size (and thus laser compression energy). This is as expected, as the deposited energy is greater relative to the hotspot energy for smaller capsules (and the base yield is much lower). Even for capsule D (the largest capsule), 10 kJ of deposited energy is sufficient to double the yield, while 60 kJ of injected energy amplifies the yield by over 12 times. The results are particularly notable for capsule A (the smallest capsule), where 10 kJ of deposited energy gives over 10 times yield amplification, and 60 kJ amplifies yield by over 80 times. It is important to note that these implosions occur within the regime identified in Paddock *et al.* (2021) and continue to satisfy the four criteria outlined in that paper, meaning that they are still expected to have low-instability growth and thus show reasonable agreement between simulation and experiment.

4.3. Burning plasma parameter for heated capsules

Estimates of Q_{α}^{tot} as a function of deposited energy for capsules A–D are displayed in figure 10. In this case, the total work done on the capsule was recorded just after the electron energy was added (slightly later than when the kinetic and thermal energies are equal, the point for which the work done was measured in § 3.3). As seen in figure 8, this remains a good estimate of the total energy of the capsule before significant alpha heating occurs. However, measuring $E_{\text{PdV}}^{\text{tot}}$ in this way also ensures that the full deposited electron energy is included in the estimate of Q_{α}^{tot} . Otherwise, Q_{α}^{tot} was calculated as in the previous section.

The results in figure 10 again show the performance achieved by these capsules. Capsules B, C and D are all shown to enter the burning plasma regime, for different amounts of deposited electron energy. This suggests the possibility of sub-MJ burning plasma (depending upon the efficiency with which the electron beams can be created and

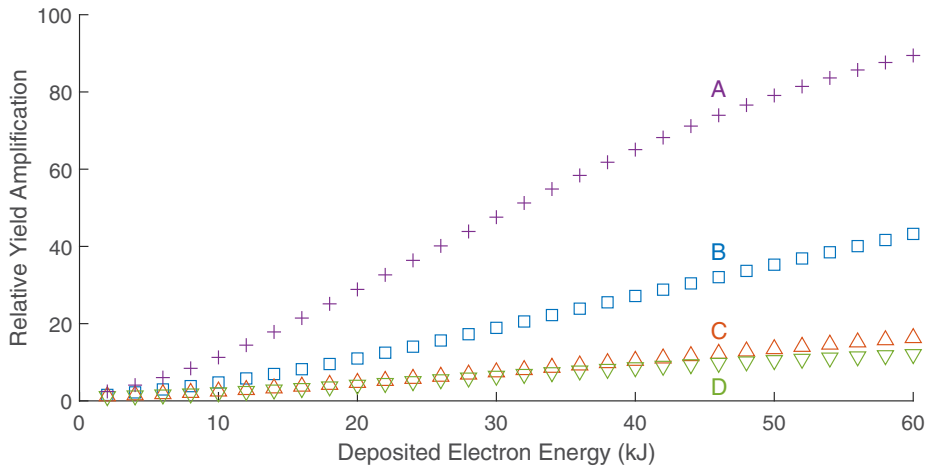


FIGURE 9. Yield amplification relative to the capsule without auxiliary heating as a function of deposited electron energy for capsules A (purple pluses), B (blue squares), C (orange upward triangles) and D (green downward triangles). The optimal time for electron deposition for each capsule was used, as determined from figure 7.

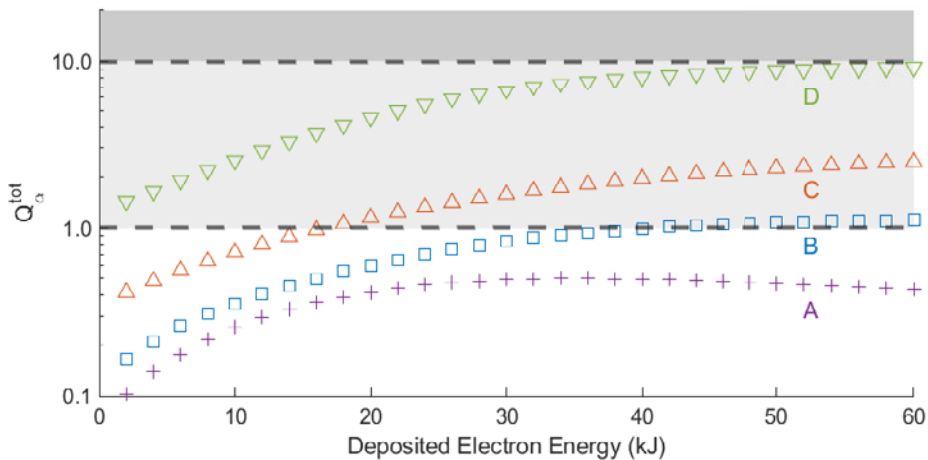


FIGURE 10. Approximate total capsule burning plasma parameter vs deposited electron energy for capsules A (purple pluses), B (blue squares), C (orange upward triangles) and D (green downward triangles). The lightly shaded region above $Q_{\alpha}^{\text{tot}} = 1$ represents the burning plasma regime, where the energy deposited by the alpha particles up to the bang time exceeds the hydrodynamic assembly energy of the capsule, while the darker shaded region indicates a rough threshold for ignition of $Q_{\alpha}^{\text{tot}} > 10$.

coupled to the hotspot). As noted previously, capsule D is already within the burning plasma regime without any electron energy added. It can also be seen that capsule D is nearing the rough ‘ignition’ threshold given by $Q_{\alpha}^{\text{tot}} = 10$ when auxiliary heating is used, once again showing the potential of this technique.

4.4. Discussion: estimating input energy and gain

The yield amplifications and capsule performance observed in previous sections suggest potential increases to capsule gain, which could be of interest for IFE applications. However, calculating the gain requires estimates of the input energy to the capsule. The total input energy for such implosions consists of two components: the long-pulse energy to provide the compression, which is measured directly from the simulations, and the short-pulse energy required to generate electron beams of sufficient energy to provide the energy deposition required for the auxiliary heating. As the short-pulse laser itself is not included within these simulations the energy requirements for the heating are not known with certainty. However, they can be approximated using best estimates for the relevant conversion efficiencies from the current literature, in order to provide estimates of what the gain of these implosions might be.

The energy deposited in the hotspot for the auxiliary heating is the value used in HYADES, and represents the known starting point. The first required conversion efficiency is the coupling between the electron beams and the electrons in the hotspot. This allows for the calculation of electron beam energy that is required in the hotspot in order to deposit the appropriate amount of energy. This efficiency was estimated in the previously discussed Vlasov–Maxwell simulations by Ratan *et al.* (2017), and found to be around 18 %.

The other key conversion efficiency required relates to how much short-pulse laser energy is needed to generate and deliver electron beams to the implosion hotspot with the required energy. Previous research has investigated how efficiently this process can be performed due to its relevance for fast ignition, and have produced a range of estimates for the efficiency with which these beams can be generated and transported (see Kemp, Sentoku & Tabak 2009; Ma *et al.* 2012; Kemp *et al.* 2014). This topic is discussed in detail in a recent review by Norreys *et al.* (2014). Two particular works are highlighted here. First is that of Strozzi *et al.* (2012), who performed particle-in-cell simulations for an ignition scale plasma. They estimated an overall laser to electron power conversion efficiency of 52 %, which they then coupled to a hydrodynamic code for fast ignition simulations. The second work of particular note for this paper is that of Tonge *et al.* (2009). They also performed particle-in-cell simulations, but observed that a significant fraction of beam energy is absorbed by the weakly collisional background plasma that the generated fast electrons must pass through in order to reach the hotspot. This led to them calculating a lower conversion efficiency of 15 %. However, it is also worth noting that Tonge *et al.* (2009) observed that the conversion efficiency increased with both laser power and the time over which the laser pulse was applied for, and the maximum simulation time of 2.5 ps that was used in that work is significantly shorter than the 7 ps over which the deposition occurs here.

In order to represent the range of uncertainty surrounding this efficiency, both the value of 52 % calculated by Strozzi *et al.* (2012) and 15 % calculated by Tonge *et al.* (2009) have been used in this work to produce estimates of the input energy. In each case, this efficiency has been combined with the value of 18 % for electron beam to hotspot coupling to estimate the total short-pulse energy required for the auxiliary heating, which has been added to the long-pulse laser energy used in the simulation to calculate the total required laser energy. These two sets of input energies have then been used to estimate the gain corresponding to the two conversion efficiencies. These gain estimates can be seen in figure 11.

The general trends are the same for both figures 11(a) and 11(b), but the results are substantially more impressive for the higher conversion efficiency. In this case, break even

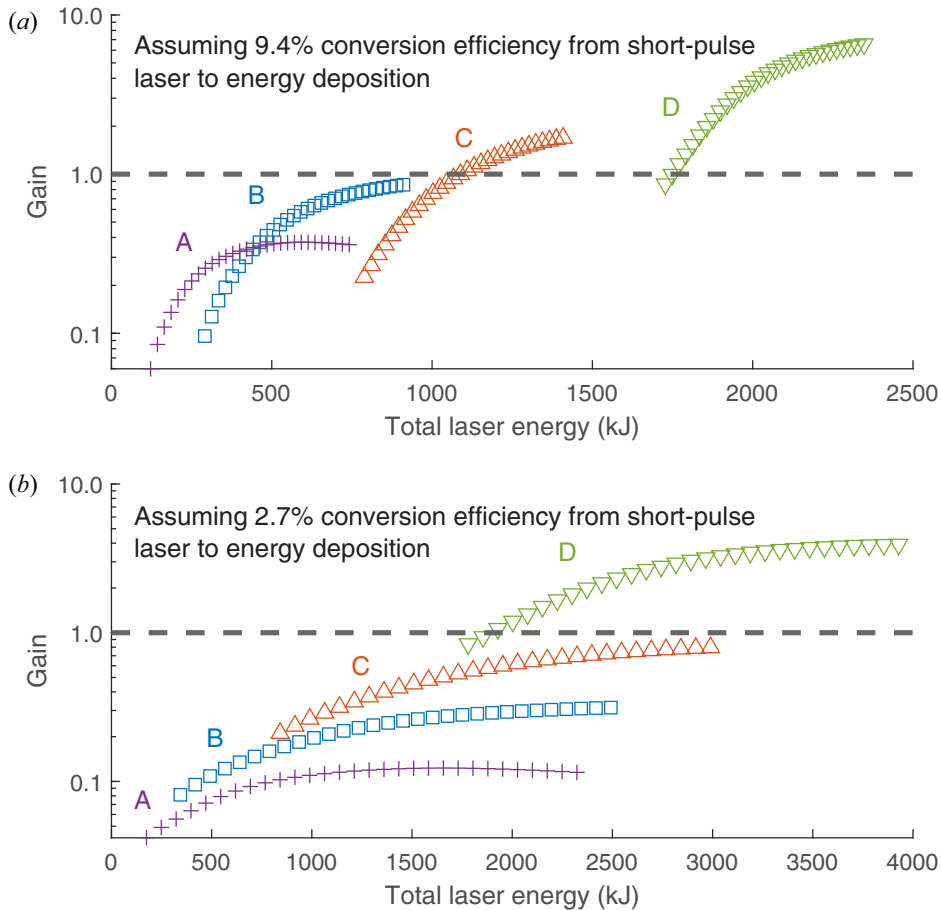


FIGURE 11. Two estimates of capsule gain vs total input energy for capsules A (purple pluses), B (blue squares), C (orange upward triangles) and D (green downward triangles). The total input energy includes the long-pulse laser energy, along with the estimated short-pulse energy required for the auxiliary heating. Both estimates assume that energy from the electron beams is deposited into the hotspot with an 18% conversion efficiency, but use different estimates for the efficiency with which the electron beams can be generated from the short-pulse laser and delivered to the hotspot. (a) Uses the estimate of 52% from Strozzi *et al.* (2012) for this efficiency (giving a total efficiency of 9.4%), while (b) uses the value of 15% from Tonge *et al.* (2009) (giving a total efficiency of 2.7%).

is achieved using capsule C for around 1.1 MJ of total input energy (using ~ 350 kJ of short-pulse laser energy to deposit 32 kJ of electron energy into the hotspot). This is a significant result, given the low energy at which it is achieved. With increased auxiliary heating energy for the same capsule, gains as high as 1.6 can be achieved for ~ 1.45 MJ of input energy (occurring for the maximum 60 kJ of deposited electron energy simulated), while using capsule D gains of up to ~ 3.5 are possible for under 2 MJ. While break even is not achieved for the smaller capsules, the gains achieved at these energies still reach ~ 0.8 at 900 kJ and ~ 0.4 at 500 kJ for capsule B, and ~ 0.35 at 500 kJ and ~ 0.2 at 250 kJ for capsule A. Given the trends seen in figure 11(a), it seems highly likely that a capsule with

size between that of B and C (i.e. with a compression energy somewhere between 270 and 800 kJ) would achieve break even for under 1 MJ of total input energy.

It is also clear from [figure 11\(a\)](#) that, for a given energy, a smaller capsule with auxiliary heating outperforms a larger capsule without (or with less) heating. This is to be expected given the conversion efficiencies involved; the laser-to-electron beam conversion of 52 % and electron beam-to-hotspot conversion of 18 % combine to give a total laser-to-hotspot coupling of over 9 %, which outperforms the efficiency of ~6 % typical for standard direct-drive implosions. This means that the auxiliary heating technique is a more efficient way of depositing energy than long-pulse irradiation, and thus better performance is expected when a greater proportion of the given energy goes into auxiliary heating. However, it is also clear that this does not continue indefinitely; the gain is seen to level off in [figure 11\(a\)](#) for higher deposited electron energies (or in the case of capsule A, eventually even reduce). This highlights the diminishing returns of this approach at higher energies (likely because both high densities and temperatures are required for high fusion yields, and at some point the density starts to become the limiting factor).

However, comparing [figures 11\(a\)](#) and [11\(b\)](#) highlights clearly how the efficiency with which the electron beams can be generated and transported to the hotspot significantly affect the gain that can be achieved using the auxiliary heating technique. The lower conversion efficiency seen in [\(b\)](#) results in only capsule D achieving break even in the range studied, at around 1.9 MJ of total energy. It is worth noting that when using the lower (15 %) laser-to-electron beam coupling efficiency, the total coupling efficiency drops to 2.7 %, meaning that auxiliary heating no longer has an efficiency advantage over the standard direct drive approach. This highlights how the viability of auxiliary heating is intrinsically linked to the efficiency with which the electron beams can be generated and deposited (although it is encouraging that, even for a low laser–electron beam coupling of 20 %, break even still occurs for under 2 MJ). Given that considerable uncertainty remains about the precise value of these conversion efficiencies, further work is required to develop these techniques in order to provide increased confidence on the potential of this approach for IFE.

4.5. Discussion: comparison with indirect-drive and NIF results

These results can be compared with those discussed in Norreys *et al.* (2021), where similar plots of yield amplification vs time and amount of electron energy deposition for a single indirect-drive capsule were produced. While there are some minor differences (the results in Norreys *et al.* (2021) demonstrate less dependence on the time of electron energy deposition than observed here, and also a lower level of yield amplification than would be expected), the change in yield amplification as a function of both time and energy displayed in [figures 7](#) and [9](#) are broadly similar to those described in Norreys *et al.* (2021). Some differences are also to be expected, given the differences in capsule design (the capsule in Norreys *et al.* (2021) had significantly lower yield and did not demonstrate significant alpha heating) and simulation code used (XRAGE, compared with HYADES). Together, these papers suggest that the auxiliary heating approach is applicable to both direct- and indirect-drive configurations and can lead to substantial amplification of fusion yields.

The auxiliary heating concept has application beyond the capsules considered in this paper, and could be used more widely to amplify fusion yields. To demonstrate this, the results from capsules A–D in this paper are applied to a series of previous NIF results. The challenges with applying auxiliary heating (and the uncertainty around the exact efficiency with which it could be applied) mean that these discussions are illustrative only, but they

demonstrate the potential of this technique and provide motivation for further study of the topic.

Capsule B in this work bears significant resemblance to NIF shots N190918, N191007 and N191110 (which at the time demonstrated record inertial fusion yields Zylstra *et al.* 2021). It should be noted, however, that these implosions were targeting higher convergence ratios of above 25, although the specific values achieved were not reported. These NIF shots produced neutron yields ranging from 0.75×10^{16} to 2×10^{16} (compared with 0.8×10^{16} for capsule B without auxiliary heating) and fuel kinetic energies of ~ 15 kJ (also similar to capsule B), for ~ 1.9 MJ of indirect-drive input energy. Based on these shots, it was predicted that ~ 3 MJ of laser energy would be required to achieve MJ-level yields (Zylstra *et al.* 2021), with other estimates suggesting that an upgrade to up to even ~ 5 MJ may be required (Cheng *et al.* 2021; Zylstra *et al.* 2021). Assuming that the similarity of these NIF capsules to capsule B means that they would demonstrate a comparable response to auxiliary heating, it is estimated that applying auxiliary heating would allow these implosions to reach the MJ level for significantly lower energies than the 3–5 MJ otherwise predicted. For instance, a deposited electron energy of 32 kJ would amplify the yield by twenty (as seen for capsule B in figure 9) for less than 350 kJ of short-pulse laser energy (assuming the 9.4 % total conversion efficiency discussed previously), achieving the targeted 1 MJ yield (since N191110 generated 56 kJ) for a total input energy of 2.3 MJ.

Since the results discussed in Zylstra *et al.* (2021) were published, a yield of 1.3 MJ has been achieved on the NIF (Bishop 2021). This is a highly significant result, and a key milestone in the quest for an IFE reactor. The yield of 1.3 MJ fits midway between that of capsules C and D, suggesting yield amplifications with deposited electron energy somewhere between the results for these capsules seen in figure 9. If the more conservative amplifications of capsule D are applied to this implosion, this suggests that the 1.3 MJ result could be doubled for 10 kJ of deposited energy, which (assuming the same conversion efficiencies) would require just over 100 kJ of short-pulse laser energy. While this is only a simple estimate that does not take into account the details of the capsule, it certainly illustrates the possibility of auxiliary heating as a technique to amplify fusion yields and provides possible motivation for researching this approach. If future work confirms these findings (and the efficiency with which electron beams can be produced and coupled to the capsule hotspots is confirmed to be high), it may be worth considering the inclusion of a short-pulse capability in future NIF upgrades or alternative high-power laser facilities.

4.6. Hotspot dynamics

The deposition of electron energy also causes some interesting behaviour within the capsule hotspot, as shown in figure 12. In the HYADES simulations, electron energy is added over 7 ps to those simulation zones corresponding to DT vapour at the start of the simulation. This energy is added according to the zone masses, meaning higher density zones receive a larger amount of energy. This injected electron energy causes a sudden increase in the electron temperature as expected, and rapidly leads to an increased ion temperature (due to the equilibration of the ions and electrons). However, there is a region of lower ion temperature which propagates from the vapour/foam boundary towards the centre of the hotspot, before disappearing. The addition of the electron energy also corresponds to an increase in pressure, which propagates away from the vapour/foam boundary in both directions, leaving behind a region of both reduced pressure and density. This also causes a brief expansion of the vapour, followed by a rapid contraction.

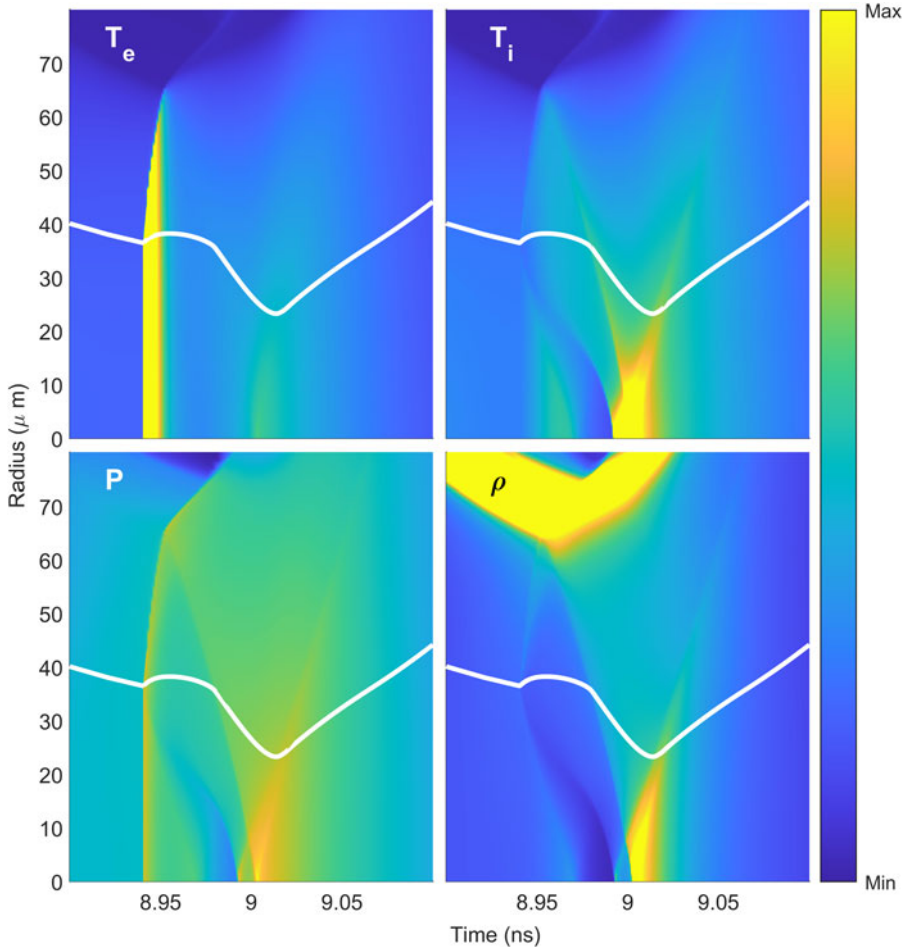


FIGURE 12. Electron temperature T_e ((a), ranging between 0–20 keV), ion temperature T_i ((b), 0–10 keV), pressure P ((c), log scale, 100–500 PPa) and density ρ ((d), 0–100 g cm⁻³) in the centre of capsule B, around the time of maximum compression, with the deposition of 20 kJ of electron energy at 8.95 ns. Pressure is displayed on a log scale, while the other 3 plots are linear in the third coordinate. High valued regions are coloured yellow while lower valued regions appear as blue, as shown on the normalised colour bar. The white line across each plot represents the boundary between vapour zones and wetted-foam zones.

A suggested explanation for this behaviour is as follows. The sudden addition of energy to the vapour zones leads to a sudden increase in temperature and pressure within this region. This same increase is not experienced in the foam regions. This drives a shock through the foam from the vapour/foam boundary, and a subsequent rarefaction wave through the vapour (explaining the movement of the boundary, the increased pressure moving through the foam and the reduction in pressure, density and temperature within the vapour). This shock continues until it encounters the high density shell, which it reflects off. It then propagates back through the foam and vapour until it reaches the centre of the capsule, driving the subsequent increase in pressure, density and temperature.

5. Conclusions

The 100 and 270 kJ capsules presented in § 2.1, including a new hydrodynamic equivalent capsule at 270 kJ, provide the option for lower energy implosions within the low-instability growth regime identified in Paddock *et al.* (2021). This is an energy scale suitable for experiments at current facilities. These experiments promise to verify the expected low-instability growth, agreement between simulation and experiment, and 1-D-like performance of the low CR regime. Success with these experiments would significantly boost confidence in this regime, and thus also in the higher-energy implosions presented previously in Paddock *et al.* (2021).

In addition, a variety of potential approaches to increase the IFE performance achievable within the low-instability regime were demonstrated. Changing the wavelength to 193 nm (achievable with ArF lasers) permits a further increase in laser power within the restrictions set by the low-instability criteria, and is seen to significantly increase capsule gain for a given energy. Using this approach, a gain greater than 10 is achieved for under 1.6 MJ, demonstrating an order of magnitude improvement over the 0.75 gain achieved in Paddock *et al.* (2021) for comparable third-harmonic energies. Two-colour implosions, where a four-pulse third-harmonic laser sequence is supplemented with a single high-power ArF pulse late in the implosion, were seen to also offer an increase in performance over third-harmonic implosions for reduced ArF energies. The exact performance and energy distribution between the two lasers varied, but results included a 2.1 MJ implosion which achieved a gain of 15.5 using less than 300 kJ of ArF pulse energy. This highlights a potential way to benefit from the increased performance achieved at higher laser frequencies, while providing the majority of the energy using conventional third-harmonic lasers.

Meanwhile, the auxiliary heating simulations presented in § 4 demonstrate how the fusion yield within the low-CR regime can potentially be significantly increased. This provides further motivation for the continued development of auxiliary heating schemes. Yield amplifications of up to 80 times (relative to the capsules without auxiliary heating) were observed in these simulations (with, as expected, the highest amplifications occurring for the smallest capsules). These results support the findings of previous work that demonstrated similarly high performance of such heating schemes for indirect-drive implosions (Norreys *et al.* 2021). The fusion performance of the capsules was also measured by approximating the value of the burning plasma parameter Q_{α}^{tot} for the simulated implosions. This showed that the three largest capsules all entered the burning plasma regime (characterised by $Q_{\alpha}^{\text{tot}} = 1$) for under 50 kJ of deposited electron energy, raising the possibility of achieving burning plasmas using this technique for sub-MJ total input energies (depending on the values of the conversion efficiencies involved in providing the heating). The largest capsule (1.8 MJ) entered the burning plasma regime even without auxiliary heating, and the addition of the extra electron energy led to Q_{α}^{tot} values approaching ten, suggesting substantial quantities of alpha heating. This again shows the promise of the implosions demonstrated in Paddock *et al.* (2021).

Two different estimates of the total gain for the simulated implosions were then produced, reflecting the uncertainty within the current literature regarding the efficiency with which electron beams can be generated and transported to the implosion hotspot. The more optimistic estimate (based on an efficiency of 52 % for the generation and transport of electron beams to the implosion hotspot, paired with the expected beam–plasma energy coupling of 18 %) suggests that break even may be possible for total laser input energies of 1.1 MJ. However, the lower estimate (replacing the 52 % value with a value of 15 %)

required an energy of ~ 2 MJ for break even, highlighting the dependence of this technique upon a high conversion efficiency.

Overall, these results demonstrate a pathway first for the low-instability regime to be tested experimentally, and secondly for the fusion performance within this regime to be significantly increased with the application of additional techniques and approaches. Paired with the results in Paddock *et al.* (2021), this work further highlights the potential contribution of the low-instability regime to IFE research.

Acknowledgements

The authors gratefully acknowledge the support of all the staff of the Central Laser Facility and the Scientific Computing Department's SCARF supercomputing facility at the UKRI-STFC Rutherford Appleton Laboratory. Useful discussions with B. Canaud, M. Farrell, J.J. Honrubia, H. Huang, J.T. Larsen, R. Ramis and W. Sweet are also gratefully acknowledged. R.W.P. acknowledges funding from UKRI-EPSC and AWE-plc through his Industrial CASE scholarship. P.A.N. acknowledges his William Penney fellowship, and the support of OxCHEDS. This work has been carried out within the framework of the EUROfusion Consortium and has received funding from the Euratom research and training programme 2019–2020 under Grant No. 633053. The views and opinions expressed herein do not necessarily reflect those of the European Commission. Work at Los Alamos National Laboratory was performed under the auspices of the U.S. Department of Energy under contract number 89233218NCA000001. This material is based upon work supported by the Department of Energy National Nuclear Security Administration under Award Number DE-NA0003856, the University of Rochester and the New York State Energy Research and Development Authority. This report was prepared as an account of work sponsored by an agency of the U.S. Government. Neither the U.S. Government nor any agency thereof, nor any of their employees, makes any warranty, express or implied or assumes any legal liability or responsibility for the accuracy, completeness or usefulness of any information, apparatus, product or process disclosed or represents that its use would not infringe privately owned rights. Reference herein to any specific commercial product, process or service by trade name, trademark, manufacturer or otherwise does not necessarily constitute or imply its endorsement, recommendation or favouring by the U.S. Government or any agency thereof. The views and opinions of authors expressed herein do not necessarily state or reflect those of the U.S. Government or any agency thereof.

Editor Luís O. Silva thanks the referees for their advice in evaluating this article.

Declaration of interests

The author report no conflict of interest.

REFERENCES

- ATZENI, S. & MEYER-TER VEHN, J. 2008 *The Physics of Inertial Fusion*. Oxford University Press.
- BETTI, R. 2011 Tutorial on the physics of inertial confinement fusion. In *3rd Meeting of the NAS Panel on Inertial Fusion Energy Systems*. https://fire.pppl.gov/IFE_NAS3_ICF_tutorial_Betti.pdf.
- BETTI, R., CHRISTOPHERSON, A.R., SPEARS, B.K., NORA, R., BOSE, A., HOWARD, J., WOO, K.M., EDWARDS, M.J. & SANZ, J. 2015 Alpha Heating and Burning Plasmas in Inertial Confinement Fusion. *Phys. Rev. Lett.* **114** (25), 255003.
- BISHOP, B. 2021 National ignition facility experiment puts researchers at threshold of fusion ignition. Lawrence Livermore National Laboratory. <https://www.llnl.gov/news/national-ignition-facility-experiment-puts-researchers-threshold-fusion-ignition>.

- CAMPBELL, E.M., GONCHAROV V.N., SANGSTER T.C., REGAN S.P., RADHA P.B., BETTI R., MYATT J.F., FROULA D.H., ROSENBERG M.J., IGUMENSHCHEV I.V., *et al.* 2017 Laser-direct-drive program: promise, challenge, and path forward. *Matter Radiat. Extrem.* **2** (2), 37–54.
- CEURVORST, L., RATAN N., LEVY M.C., KASIM M.F., SADLER J., SCOTT R.H., TRINES R.M., HUANG T.W., SKRAMIC M., VRANIC M., *et al.* 2016 Mitigating the hosing instability in relativistic laser-plasma interactions. *New J. Phys.* **18** (5), 053023.
- CHENG, B., BRADLEY, P.A., FINNEGAN, S.M. & THOMAS, C.A. 2021 Fundamental factors affecting thermonuclear ignition. *Nucl. Fusion* **61**, 096010.
- CHRISTOPHERSON, A.R., BETTI, R., BOSE, A., HOWARD, J., WOO, K.M., CAMPBELL, E.M., SANZ, J. & SPEARS, B.K. 2018 A comprehensive alpha-heating model for inertial confinement fusion. *Phys. Plasmas* **25** (1), 012703.
- CHRISTOPHERSON, A.R., BETTI, R., MILLER, S., GOPALASWAMY, V., MANNION, O.M. & CAO, D. 2020 Theory of ignition and burn propagation in inertial fusion implosions. *Phys. Plasmas* **27** (5), 052708.
- EIMERL, D., CAMPBELL E.M., KRUPKE W.F., KRUPKE J., KRUEER W.L., MAROZAS J., ZUEGEL J., MYATT J., KELLY J., FROULA D., *et al.* 2014 StarDriver: a flexible laser driver for inertial confinement fusion and high energy density physics. *J. Fusion Energ.* **33** (5), 476–488.
- FOLLETT, R.K., SHAW, J.G., MYATT, J.F., PALASTRO, J.P., SHORT, R.W. & FROULA, D.H. 2018 Suppressing two-plasmon decay with laser frequency detuning. *Phys. Rev. Lett.* **120** (13), 135005.
- GONCHAROV, V.N., REGAN S.P., SANGSTER T.C., BETTI R., BOEHLY T.R., CAMPBELL E.M., DELETTREZ J.A., EDGELL D.H., EPSTEIN R., FORREST C.J., *et al.* 2016 Demonstrating ignition hydrodynamic equivalence in direct-drive cryogenic implosions on OMEGA. *J. Phys.: Conf. Ser.* **717** (1), 012008.
- HAINES, B.M., OLSON R.E., SWEET W., YI S.A., ZYLSTRA A.B., BRADLEY P.A., ELSNER F., HUANG H., JIMENEZ R., KLINE J.L., *et al.* 2019 Robustness to hydrodynamic instabilities in indirectly driven layered capsule implosions. *Phys. Plasmas* **26** (1), 012707.
- HAINES, B.M., YI S.A., OLSON R.E., KHAN S.F., KYRALA G.A., ZYLSTRA A.B., BRADLEY P.A., PETERSON R.R., KLINE J.L., LEEPER R.J., *et al.* 2017 The effects of convergence ratio on the implosion behavior of DT layered inertial confinement fusion capsules. *Phys. Plasmas* **24** (7), 072709.
- HOHENBERGER, M., RADHA P.B., MYATT J.F., LE PAPE S., MAROZAS J.A., MARSHALL F.J., MICHEL D.T., REGAN S.P., SEKA W., SHVYDKY A., *et al.* 2015 Polar-direct-drive experiments on the national ignition facility. *Phys. Plasmas* **22** (5), 056308.
- KATO, Y., AZECHI H., TAKABE H., MIYANAGA N., KANABE T., NORIMATU T., NISHIMURA H., SHIRAGA H., NAKAI M., KODAMA R., *et al.* 2008 Implosion experiments with uniformity-improved GEKKO XII: overview. *AIP Conf. Proc.* **369**, 101–107.
- KEHNE, D.M., KARASIK, M., AGLITSKY, Y., SMYTH, Z., TERRELL, S., WEAVER, J.L., CHAN, Y., LEHMBERG, R.H. & OBENSCHAIN, S.P. 2013 Implementation of focal zooming on the Nike KrF laser. *Rev. Sci. Instrum.* **84** (1), 013509.
- KEMP, A.J., FIUZA, F., DEBAYLE, A., JOHZAKI, T., MORI, W.B., PATEL, P.K., SENTOKU, Y. & SILVA, L.O. 2014 Laser-plasma interactions for fast ignition. *Nucl. Fusion* **54** (5), 054002.
- KEMP, A.J., SENTOKU, Y. & TABAK, M. 2009 Hot-electron energy coupling in ultraintense laser-matter interaction. *Phys. Rev. E* **79** (6), 066406.
- KHAN S.F., MACLAREN S.A., SALMONSON J.D., MA T., KYRALA G.A., PINO J.E., RYGG J.R., FIELD J.E., TOMMASINI R., RALPH J.E., *et al.* 2016 Symmetry tuning of a near one-dimensional 2-shock platform for code validation at the National Ignition Facility. *Phys. Plasmas* **23** (4), 042708.
- KIRKWOOD R.K., TURNBULL D.P., CHAPMAN T., WILKS S.C., ROSEN M.D., LONDON R.A., PICKWORTH L.A., COLAITIS A., DUNLOP W.H., POOLE P., *et al.* 2018a A plasma amplifier to combine multiple beams at NIF. *Phys. Plasmas* **25** (5), 56701.
- KIRKWOOD R.K., TURNBULL D.P., CHAPMAN T., WILKS S.C., ROSEN M.D., LONDON R.A., PICKWORTH L.A., DUNLOP W.H., MOODY J.D., STROZZI D.J., *et al.* 2018b Plasma-based beam combiner for very high fluence and energy. *Nat. Phys.* **14** (1), 80–84.
- LARSEN, J.T. & LANE, S.M. 1994 HYADES-A plasma hydrodynamics code for dense plasma studies. *J. Quant. Spectrosc. Radiat. Transfer* **51** (1–2), 179–186.

- LE PAPE S., DIVOL L., BERZAK HOPKINS L., MACKINNON A., MEEZAN N.B., CASEY D., FRENJE J., HERRMANN H., MCNANEY J., MA T., *et al.* 2014 Observation of a reflected shock in an indirectly driven spherical implosion at the National Ignition Facility. *Phys. Rev. Lett.* **112** (22), 225002.
- LI C.K., SÉGUIN F.H., FRENJE J.A., KUREBAYASHI S., Petrasso R.D., Meyerhofer D.D., Soures J.M., Delettrez J.A., Glebov V.Y., Radha P.B., *et al.* 2002 Effects of fuel-shell mix upon direct-drive, spherical implosions on OMEGA. *Phys. Rev. Lett.* **89** (16), 165002.
- LINDL, J. 1995 Development of the indirect-drive approach to inertial confinement fusion and the target physics basis for ignition and gain. *Phys. Plasmas* **2** (11), 3933–4024.
- LINDL, J.D., AMENDT, P., BERGER, R.L., GLENDINNING, S.G., GLENZER, S.H., HAAN, S.W., KAUFFMAN, R.L., LANDEN, O.L. & SUTER, L.J. 2004 The physics basis for ignition using indirect-drive targets on the national ignition facility. *Phys. Plasmas* **11** (2), 339–491.
- LINDL J.D., LANDEN O.L., EDWARDS J., MOSES E.I., ADAMS J., AMENDT P.A., ANTIPA N., ARNOLD P.A., ASHABRANNER R.C., ATHERTON L.J., *et al.* 2014 Review of the national ignition campaign 2009–2012. *Phys. Plasmas* **21** (2), 020501.
- MA T., SAWADA H., PATEL P.K., CHEN C.D., DIVOL L., HIGGINSON D.P., KEMP A.J., KEY M.H., LARSON D.J., LE PAPE S., *et al.* 2012 Hot electron temperature and coupling efficiency scaling with prepulse for cone-guided fast ignition. *Phys. Rev. Lett.* **108** (11), 115004.
- MEYERHOFER D.D., DELETTREZ J.A., EPSTEIN R., GLEBOV V.Y., GONCHAROV V.N., KECK R.L., MCCRORY R.L., MCKENTY P.W., MARSHALL F.J., RADHA P.B., *et al.* 2001 Core performance and mix in direct-drive spherical implosions with high uniformity. *Phys. Plasmas* **8** (5), 2251.
- MONTGOMERY, D.S. 2016 Two decades of progress in understanding and control of laser plasma instabilities in indirect drive inertial fusion. *Phys. Plasmas* **23** (5), 055601.
- NISHIMURA H., SHIRAGA H., AZECHI H., MIYANAGA N., NAKAI M., IZUMI N., NISHIKINO M., HEYA M., FUJITA K., OCHI Y., *et al.* 2000 Indirect-direct hybrid target experiments with the GEKKO XII laser. *Nuclear Fusion* **40**, 547.
- NORA R., BETTI R., ANDERSON K.S., SHVYDKY A., BOSE A., WOO K.M., CHRISTOPHERSON A.R., MAROZAS J.A., COLLINS T.J., RADHA P.B., *et al.* 2014 Theory of hydro-equivalent ignition for inertial fusion and its applications to omega and the national ignition facility. *Phys. Plasmas* **21**.
- NORREYS, P.A., CEURVORST L., SADLER J.D., SPIERS B.T., ABOUSHELBAZA R., MAYR M.W., PADDOCK R., RATAN N., SAVIN A.F., WANG R.H.W., *et al.* 2021 Preparations for a European R&D roadmap for an inertial fusion demo reactor. *Phil. Trans. R. Soc. A* **379** (2189), 20200005.
- NORREYS P., BATANI D., BATON S., BEG F.N., KODAMA R., NILSON P.M., PATEL P., PEREZ F., SANTOS J.J., SCOTT R.H., *et al.* 2014 Fast electron energy transport in solid density and compressed plasma. *Nucl. Fusion* **54** (5), 054004.
- NUCKOLLS, J.H. 2010 Grand challenges of inertial fusion energy. *J. Phys.: Conf. Ser.* **244**, 012007.
- OBENSCHAIN, S.P., SCHMITT, A.J., BATES, J.W., WOLFORD, M.F., MYERS, M.C., MCGEOCH, M.W., KARASIK, M. & WEAVER, J.L. 2020 Direct drive with the argon fluoride laser as a path to high fusion gain with sub-megajoule laser energy. *Phil. Trans. R. Soc. A* **378** (2184), 20200031.
- OLSON R.E., LEEPER R.J., KLINE J.L., ZYLSTRA A.B., YI S.A., BIENER J., BRAUN T., KOZIOZIEMSKI B.J., SATER J.D., BRADLEY P.A., *et al.* 2016 *First liquid layer inertial confinement fusion implosions at the National Ignition Facility* **117** (24), 245001.
- PADDOCK, R.W., MARTIN H., RUSKOV R.T., SCOTT R.H.H., GARBETT W., HAINES B.M., ZYLSTRA A.B., ABOUSHELBAZA R., MAYR M.W. & SPIERS B.T., *et al.* 2021 One-dimensional hydrodynamic simulations of low convergence ratio direct-drive inertial confinement fusion implosions. *Phil. Trans. R. Soc. A* **379** (2189), 20200224.
- RATAN, N., SIRCOMBE, N.J., CEURVORST, L., SADLER, J., KASIM, M.F., HOLLOWAY, J., LEVY, M.C., TRINES, R., BINGHAM, R. & NORREYS, P.A. 2017 Dense plasma heating by crossing relativistic electron beams. *Phys. Rev. E* **95** (1), 013211.
- SKUPSKY, S., MAROZAS J.A., CRAXTON R.S., BETTI R., COLLINS T.J., DELETTREZ J.A., GONCHAROV V.N., MCKENTY P.W., RADHA P.B., BOEHLI T.R., *et al.* 2004 Polar direct drive on the national ignition facility. *Phys. Plasmas* **11**, 2763.
- SMALYUK, V.A., WEBER C.R., LANDEN O.L., ALI S., BACHMANN B., CELLIERS P.M., DEWALD E.L., FERNANDEZ A., HAMMEL B.A., HALL G., *et al.* 2020 Review of hydrodynamic instability

- experiments in inertially confined fusion implosions on national ignition facility. *Plasma Phys. Control. Fusion* **62** (1), 014007.
- SPIERS, B.T., HILL M.P., BROWN C., CEURVORST L., RATAN N., SAVIN A.F., ALLAN P., FLOYD E., FYRTH J., HOBBS L., *et al.* 2021 Whole-beam self-focusing in fusion-relevant plasma. *Phil. Trans. R. Soc. A* **379** (2189), 20200159.
- STROZZI, D.J., TABAK, M., LARSON, D.J., DIVOL, L., KEMP, A.J., BELLEI, C., MARINAK, M.M. & KEY, M.H. 2012 Fast-ignition transport studies: realistic electron source, integrated particle-in-cell and hydrodynamic modeling, imposed magnetic fields. *Phys. Plasmas* **19** (7), 072711.
- TONGE, J., MAY, J., MORI, W.B., FIUZA, F., MARTINS, S.F., FONSECA, R.A., SILVA, L.O. & REN, C. 2009 A simulation study of fast ignition with ultrahigh intensity lasers. *Phys. Plasmas* **16**, 056311.
- TYNAN, G.R. & ABDULLA, A. 2020 How might controlled fusion fit into the emerging low-carbon energy system of the mid-twenty-first century? *Phil. Trans. R. Soc. A* **378** (2184), 20200009.
- WALTERS, C., ALGER E., BHANDARKAR S., BOEHM K., BRAUN T., ESPINOSALOZA F., HAID B., HEREDIA R., KLINE J., KOZIOZIEMSKI B., *et al.* 2018 D2 and d-T liquid-layer target shots at the national ignition facility. *Fusion Sci. Technol.* **73** (3), 305–314.
- ZYLSTRA, A.B., KRITCHER A.L., HURRICANE O.A., CALLAHAN D.A., BAKER K., BAKER T., CASEY D.T., CLARK D., CLARK K., DÖPPNER T., *et al.* 2021 Record energetics for an inertial fusion implosion at NIF. *Phys. Rev. Lett.* **126** (2), 025001.
- ZYLSTRA, A.B., YI S.A., HAINES B.M., OLSON R.E., LEEPER R.J., BRAUN T., BIENER J., KLINE J.L., BATHA S.H., BERZAK HOPKINS L., *et al.* 2018 Variable convergence liquid layer implosions on the National Ignition Facility. *Phys. Plasmas* **25** (5), 056304.